THE JOURNAL OF PHYSICAL CHEMISTRY C

Article

pubs.acs.org/JPCC

Electronic Structure and Comparative Properties of $LiNi_xMn_yCo_zO_2$ Cathode Materials

Hong Sun and Kejie Zhao*

School of Mechanical Engineering, Purdue University, West Lafayette, Indiana 47906, United States

Supporting Information

ABSTRACT: We study the electronic structure and valence states in $LiNi_xMn_yCo_zO_2$ (NMC) materials and compare the resulting electronic, structural, mechanical, and thermal properties of a class of NMC compositions. The Jahn−Teller distortion in the transition metal (TM) octahedral complex allows us to determine the ionic states of the TM elements. The variation of Ni^{2+}/Ni^{3+} and Co^{2+}/Co^{3+} as the NMC composition changes alters the structural stability, electrical conductivity, lattice parameters, elastic modulus, and thermal stability. The theoretical predictions are in excellent agreement with the experimental results. Through intensive computational screening, we further show that long-range atomic ordering is absent in the NMC lattice due to the mixture of the ionic states and similar ionic radii of the TM elements. The first-principles modeling provides a theoretical foundation on a complete understanding of the physicochemical properties of NMC at the level of electronic structures.

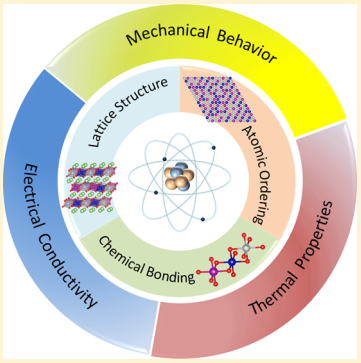

INTRODUCTION

Electrification of automotive transportation and integration of renewable energies constitute two critical pathways toward reduction of gas emissions and mitigation of environmental risks.[1] These imperative demands incur challenges in terms of energy storage technologies, for which Li-ion batteries emerge as a versatile and efficient option. $LiNi_xMn_yCo_zO_2$ $(x + y + z = 1)$ is the state-of-the-art choice of cathode materials for high-capacity Li-ion batteries in the electric vehicle applications.[2,3] NMC is formed by partially replacing Co in $LiCoO_2$ by Ni and Mn to achieve the improved electrochemical performance while reducing the material cost.[4] The composition of Ni, Mn, and Co can be tuned to optimize the capacity, cyclic rate, electrochemical stability, and lifetime.

The class of NMC materials has the same hexagonal α-$NaFeO_2$ ($R3m$) structure, where Li, O, and transition metals (TMs) occupy alternating atomic layers, and the TM elements reside at the center of the O octahedron.[5] Ni, Mn, and Co contribute to the enhanced performance of NMC in different ways. Ni-rich compositions demonstrate high discharge capacity;[6] Mn-rich compositions maintain better cycle life and thermal safety; while Co-rich compositions provide excellent rate capability.[7] On the other hand, the addition of Ni and Mn is also associated with different challenges; for instance, Ni-rich cathode suffers from structural degradation during cycles because of the Ni mixing with the Li sites, while Mn-rich material has a reduced capacity because of the inactivity of Mn^{4+} during Li reactions.[8,9] Therefore, there is ample room to optimize the composition of the ternary material NMC to reach a balanced behavior among the capacity, rate capability, structural stability, and cyclability.

This paper studies the electronic structure and valence states in NMC and compares the resulting electronic, structural, mechanical, and thermal properties of a class of NMC materials based on the first-principles theoretical calculations. We select five different NMC compositions, $LiNi_{1/3}Mn_{1/3}Co_{1/3}O_2$ (NMC333), $LiNi_{0.4}Mn_{0.4}Co_{0.2}O_2$ (NMC442), $LiNi_{0.5}Mn_{0.3}Co_{0.2}O_2$ (NMC532), $LiNi_{0.6}Mn_{0.2}Co_{0.2}O_2$ (NMC622), and $LiNi_{0.8}Mn_{0.1}Co_{0.1}O_2$ (NMC811), to systematically vary the composition of the TM elements and map their physicochemical properties. We determine the ionic states of Ni^{2+}/Ni^{3+}, Co^{2+}/Co^{3+}, and Mn^{3+}/Mn^{4+} by examining the Jahn−Teller (JT) distortion of the TM−O octahedral complex. The occupation fractions of Ni^{2+}/Ni^{3+} and Co^{2+}/Co^{3+} vary as the NMC composition changes which leads to the alternation of the electronic properties, lattice parameters, mechanical properties, as well as the thermal stability. The theoretical predictions are in excellent agreement with the existing experimental results. Furthermore, the superlattice ordering in NMC is largely unknown which prohibits the implementation of atomistic models of NMC. We screen 81 configurations for each composition and conclude that there is no long-range atomic ordering in the TM layer due to the mixture of ionic states and similar ionic radii of the TM elements.

COMPUTATIONAL METHODS

Supercell Model. The supercell models are built using the Vienna Ab-initio Simulation Package (VASP).[10,11] The NMC supercell is constructed with the $R3m$ space group, where Li, O, and TM occupy the 3*b*, 6*c*, and 3*a* sites, respectively. 120 atoms are contained for each NMC composition. Projector-augmented-wave (PAW) potentials are used to mimic the ionic cores, while

Received: January 25, 2017
Published: February 28, 2017

DOI: 10.1021/acs.jpcc.7b00810
J. Phys. Chem. C 2017, 121, 6002−6010

the generalized gradient approximation (GGA) in the Perdew–Burke–Ernzerhof (PBE) flavor is employed for the exchange and correlation functional. To model the Coulombic repulsion between localized electrons in TMs, the DFT + U method is adopted. The Hubbard $U - J$ values for Ni, Mn, and Co are set as 6.7, 4.2, and 4.91, respectively.[12] The plane-wave set is expanded within an energy cutoff of 520 eV. The $2 \times 1 \times 1$ mesh of k points in the Monkhorst–Pack scheme is chosen for the Brillouin zone sampling. Energy optimization is considered complete when the magnitude of force per atom is smaller than 0.04 eV/Å.

Virtual Crystalline Approximation (VCA) Method. The VCA method significantly reduces the computational expense and smoothly handles all complicated stoichiometric portions of compositions. The VCA model for NMC contains 6 O atoms, 3 Li atoms, and 3 virtual TM atoms whose pseudopotentials are constructed within the first-principles VCA scheme. In the calculations of mechanical properties, electronic structure, and thermal properties, the VCA models built by ABINIT and CASTEP are adopted. In ABINIT, norm-conserving pseudopotentials generated by the Troullier–Martins method and local density approximation (LDA) of exchange correlation functional are used. A k-point mesh of $6 \times 6 \times 2$ in the Monkhorst–Pack scheme is adopted for Brillouin zone sampling. The first self-consistent convergence is achieved within an energy cutoff of 50 hartree when the tolerant potential residual $V(r)$ is less than 1.0×10^{-18} Hartree. Before calculation, optimization of atom positions is done using the conjugated gradient method until the maximum force per atom is less than 1×10^{-6} Hartree/Bohr. In CASTEP, the ultrasoft pseudopotentials are expanded within a plane-wave cutoff energy of 550 eV, and generalized gradient approximation of PBE is described as the exchange-correlation functional. The k-point of $6 \times 6 \times 2$ mesh is used in Brillouin zone sampling.

Generation of 81 Configurations for Each NMC Composition. We adopt the structural evolutional algorithm implemented in USPEX to create a series of different configurations for each NMC composition. The NMC lattice with $R3m$ space group built by VASP is used as the seed structure. The successive 80 structures for each NMC composition are developed by four evolutional generations using the merely permutation method, which randomly swaps the atomic positions of Ni, Mn, and Co in the lattice. Every structure created by USPEX is input and relaxed in VASP to obtain the free energy.

COOP Analysis. The COOP analysis is implemented in the LOBSTER tool which generates the overlap population-weighted density of states by processing the electronic-structure output from the self-consistent simulations in VASP.

Density of States. Total density of states is calculated using the smearing technique with a smearing parameter of 0.005 Ha. Partial density of states for Li, O, and TM are plotted based on the tetrahedron method using a nonshifted k-point grid in the whole Brillouin zone. Phonon frequencies are obtained by diagonalizing the dynamical matrix based on the density functional perturbation theory (DFPT). To compute the phonon band structure and phonon density of states in the Brillouin zone, an elaborate Fourier interpolation of force constants is used by a $4 \times 4 \times 2$ k-point sampling.

Mechanical Properties. In the supercell model, we employ the uniaxial tension simulation in the three directions and calculate the average Young's modulus from the slope of the stress–strain curves. In order to avoid the uncertainty due to the structural deviation, five different atomic configurations for each NMC composition are adopted in VASP. In the VCA model, the matrix of elastic constants is calculated based on the elastic response with respect to the displacement perturbation in the full set of directions. The Voigt–Reuss scheme is employed to obtain the mechanical properties.[13] According to the Voigt approximation, bulk and shear modulus are obtained by

$$B_V = \frac{1}{9}\{2(C_{11} + C_{22}) + 4C_{13} + C_{33}\}$$

$$G_V = \frac{1}{30}\{C_{11} + C_{12} + 2C_{33} - 4C_{13} + 12C_{44} + 12C_{66}\}$$

In terms of the Reuss approximation

$$B_R = \{(C_{11} + C_{12})C_{33} - 2C_{12}^2\}/(C_{11} + C_{12} + 2C_{33} - 4C_{13}\}$$

$$G_R = \left(\frac{5}{2}\right)\{[(C_{11} + C_{12})C_{33} - 2C_{12}^2]C_{55}C_{66} / \{3B_V C_{55}C_{66} + [(C_{11} + C_{12})C_{33} - 2C_{12}^2]^2(C_{55} + C_{66})\}$$

Based on the above approximation, we obtain the effective moduli $B = \frac{1}{2}(B_V + B_R)$, $G = \frac{1}{2}(G_V + G_R)$.

Young's modulus is further calculated as

$$Y = 9BG/(3B + G)$$

Thermal Properties. Based on the phonon structure, thermal properties are calculated by the finite volume method using the quasi-harmonic approximation according to the following equations[30]

$$F = 3nNk_BT \int_0^{\omega_{max}} \ln\left\{2 \sinh\left(\frac{\hbar\omega}{2k_BT}\right)\right\} g(\omega)d\omega$$

$$S = 3nNk_B \int_0^{\omega_{max}} \left[\left(\frac{\hbar\omega}{2k_BT}\right)\coth\left(\frac{\hbar\omega}{2k_BT}\right) - \ln\left\{2 \sinh\left(\frac{\hbar\omega}{2k_BT}\right)\right\}\right] g(\omega)d\omega$$

$$C_V = 3nNk_B \int_0^{\omega_{max}} \left(\frac{\hbar\omega}{2k_BT}\right)^2 \operatorname{csc} h^2\left(\frac{\hbar\omega}{2k_BT}\right) g(\omega)d\omega$$

RESULTS AND DISCUSSION

Figure 1 shows the ionic radius and 3d electron population of the six TM ions,[15] Ni^{2+}/Ni^{3+}, Co^{2+}/Co^{3+}, and Mn^{3+}/Mn^{4+}. The size of the TM ions can be generally divided into two groups. The TM elements with low oxidation states (Ni^{2+}, Co^{2+}, Mn^{3+}) have similar ionic radius in the rage of 64–69 pm, while the high oxidation states (Ni^{3+}, Co^{3+}, Mn^{4+}) are associated with smaller radius of 53–56 pm. Figure 1 also shows that the 3d orbital electron population splits into the eg^* level with a higher energy and the $t2g$ level with a lower energy due to the σ interaction between TMs and O and the JT distortion effect.[16] The low-spin (LS) Co^{3+}, Ni^{2+}, and Mn^{4+} are inactive JT ions. In comparison, the low-spin Ni^{3+}, low-spin Co^{2+}, and high-spin (HS) Mn^{3+} with a singly occupied orbital at the eg^* level are active JT species.

The oxidation state of TM elements determines the JT effect as well as the TM–O bond length. Figure 2(a) shows the atomic lattice of NMC. The TM elements reside at the octahedral site surrounded by six O atoms. Figure 2(b) shows the local view of five representative TM–O octahedral complexes in the NMC lattice.

DOI: 10.1021/acs.jpcc.7b00810
J. Phys. Chem. C 2017, 121, 6002–6010

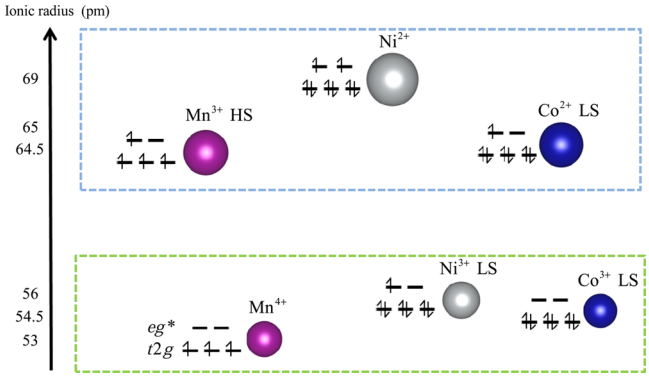

Figure 1. Ionic radius and 3d electron population of the six transition metal ions.

Because of the multivalence state of Ni, Co, and Mn cations, different TM−O bond lengths coexist for each TM element. We find that the TM−O bond length can be roughly divided into two groups, long bonds which are above 2.0 Å and short ones below 1.98 Å. The octahedra of inactive JT ions (Co^{3+}, Ni^{2+}, Mn^{4+}) are of the similar bond length in the 4-fold symmetry axes, while the active JT ions (Co^{2+}, Ni^{3+}, Mn^{3+}) distort the octahedral complexes in one of the three 4-fold symmetry axes—the short and long bonds coexist in the TM−O octahedra, as shown in Figure 2(b). Specifically, one of the 4-fold axes in the Co^{2+} octahedron shortens, while one axis in the Ni^{3+} octahedron elongates, to form the distorted complexes. The bond length analysis and JT distortion in the TM−O octahedral complexes allow us to determine the ionic states of the TM elements. We perform radial distribution function analyses using a cutoff distance of 2.2 Å to calculate the population of the short and long TM−O bonds in the five NMC compositions. As shown in Table 1, all the Mn−O bonds are short bonds of the length 1.94−1.96 Å, indicating that the Mn valence state is exclusively Mn^{4+}. Based on the populated percentages of the short and long bonds of Ni−O and Co−O, we can determine the occupation fractions of Ni^{2+}/Ni^{3+} and Co^{2+}/Co^{3+} in the five NMC compositions.

Figure 3 shows the occupation percentage of the Ni and Co cations as the NMC composition varies. In NMC333, NMC442, and NMC532, Ni^{2+} is predominant over Ni^{3+}, indicating an enhanced structural stability in the three compounds. As Ni content increases, the occupation of Ni^{3+} steadily increases at the cost of Ni^{2+}. The Ni^{3+} fraction is up to 58% in NMC811, and the large fraction of Ni^{3+} will deteriorate the structural stability in the Ni-rich compounds. This may explain the common observation that the high Ni-content NMC is more vulnerable to structural degradation—a mechanism in addition to the Li/Ni disorder effect in the electrochemical cycles. It is also worth pointing out that Ni occupies the largest portion among the three TM elements in NMC materials. The variation of the Ni valence state will predominantly control the overall physicochemical properties of NMC cathodes. For Co, when the Ni composition increases, the fraction of Co^{3+} first decreases until it reaches

Table 1. Population of the Short (S) and Long (L) TM−O Bonds in the Five NMC Compositions

	Ni−O		Co−O		Mn−O
NMC	S	L	S	L	S
333	0%	100%	86%	14%	100%
442	2%	98%	80%	20%	100%
532	8%	92%	64%	36%	100%
622	24%	76%	70%	30%	100%
811	38%	62%	100%	0%	100%

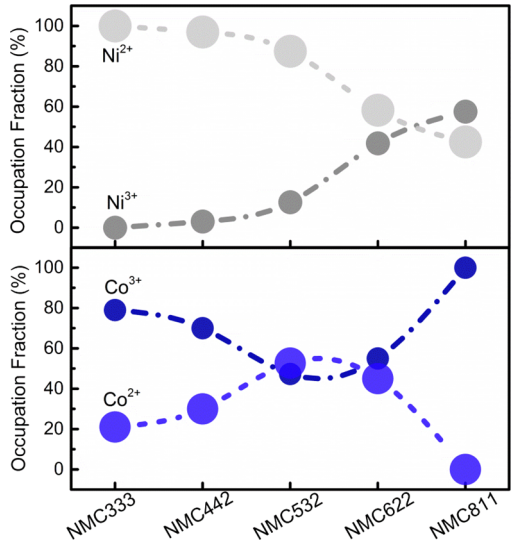

Figure 3. Occupation fraction of Ni^{2+}/Ni^{3+} and Co^{2+}/Co^{3+} in the five NMC compositions.

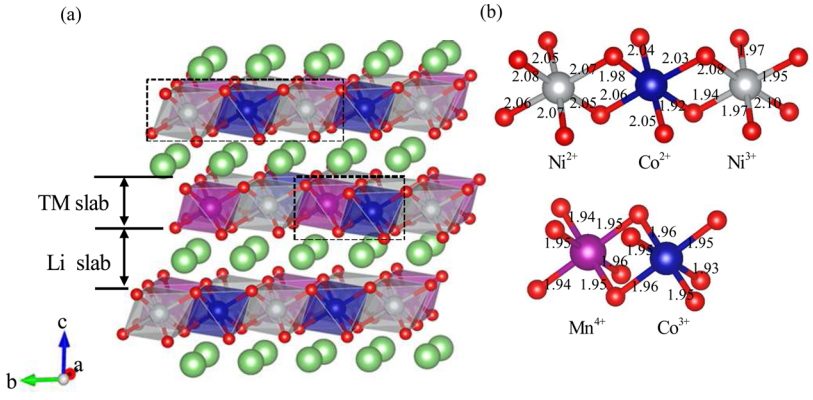

Figure 2. TM−O octahedral complexes in NMC. (a) Ni, Mn, and Co reside at the octahedral site surrounded by six O atoms. (b) Local view of the TM−O octahedral complexes. Ni^{3+} and Co^{2+} are active Jahn−Teller ions. Ni^{2+}, Co^{3+}, and Mn^{4+} are inactive Jahn−Teller species. The degree of distortion of the octahedra indicates the ionic states of the TM elements. The gray, blue, and purple spheres represent Ni, Co, and Mn atoms in the TM layer, respectively, and the red sphere represents O atoms.

DOI: 10.1021/acs.jpcc.7b00810
J. Phys. Chem. C 2017, 121, 6002−6010

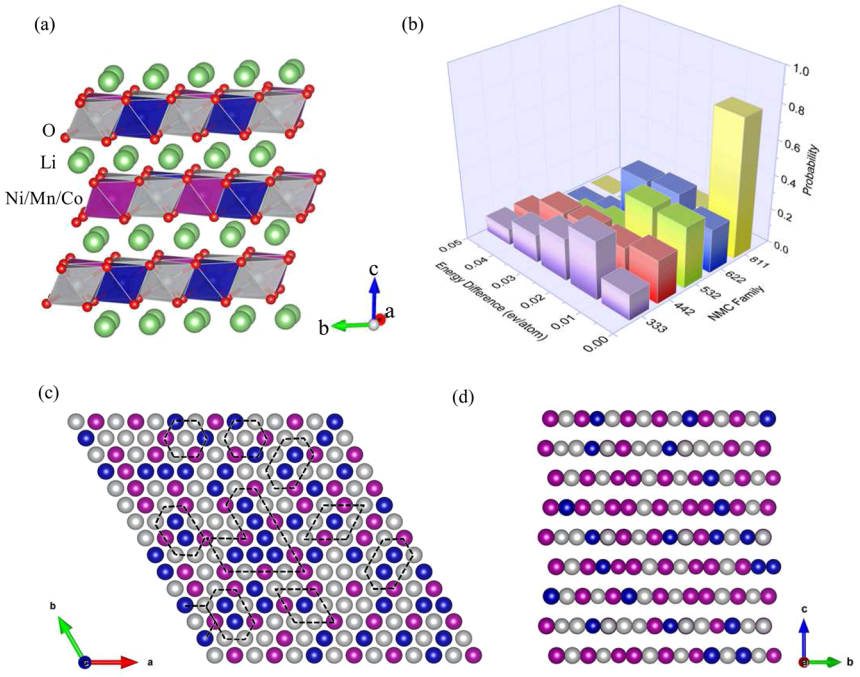

Figure 4. (a) NMC lattice with the *R*3*m* space group. (b) Population map of the 81 configurations for each NMC. Different configurations are made of different arrangements of Ni/Mn/Co in the TM layer. 81 configurations are constructed for each NMC composition and are categorized in five groups according to the difference of free energy per atom relative to the lowest energy state. Atomic arrangement from (c) the top-view and (d) the *a*-axis view of the TM layer in a NMC supercell consisting of 36 energetically favorable configurations. The dashed lines mark the possible cluster units. Multiple clusters with random population indicate the absence of long-range atomic ordering. The gray, blue, and purple spheres represent Ni, Co, and Mn atoms, respectively.

minimum in NMC532 and then gradually increases in NMC622 and NMC811. The occupation of Co^{2+} shows the opposite behavior with a maximum fraction in NMC532. From the above analysis, we learn that NMC333, with the dominant inactive JT cations Ni^{2+} and Co^{3+}, possesses much improved structural stability over other compositions.

The atomic arrangement in the NMC lattice is elusive in the literature. Based on the above analysis of the fractional occupation of TM cations, we expect that the coexistence of the aliovalent ions and similar ionic radii (Figure 1) would suppress the long-range atomic ordering in the TM layer of NMC. Figure 4(a) shows the supercell structure of NMC with the space group *R*3*m*. The supercell contains 120 atoms with an alternative sequence of Li−O−TM layers along the *c*-axis. To explore the atomic ordering in the TM layer, we construct 81 distinct configurations for each NMC composition (details in the Computational Method section) and screen their energetics. In each configuration, the Ni, Mn, and Co sites are randomly assigned in the TM layer using the USPEX program.[17] We perform the energetic relaxation and classify the 81 configurations into five groups based on the energy difference per atom relative to lowest-energy configuration. In Figure 4(b), each column represents the probability of NMC configurations within a given interval. In general, the maximum energy difference per atom in the overall 81 configurations for each composition is less than 0.05 eV. Considering that the average energy per atom in the supercell is around 5.5 eV, the small energy difference per atom (less than 1%) among the 81 configurations indicates that the random arrangement of TM elements gives similar thermodynamics states of NMC. More specifically, the configuration population shows more even distribution for NMC333 and NMC442 due to the similar portions of Ni, Mn, and Co, which may provide more possibilities of atomic mixing. When the Ni content increases, most configurations are located in the regime of the small energy difference less than 0.03 eV, which may result from the similar coordination environment where Ni is dominant. It is clear that there is not a single favorable pattern of Ni, Mn, and Co, of long-range ordering, in the TM layer in the NMC supercell. We show the top-view (Figure 4(c)) and the *a*-axis view (Figure 4(d)) of the atomic arrangement in the TM layer in a $7 \times 3 \times 3$ supercell using a cluster expansion approach[18] that consists of 36 energetically favorable configurations of NMC532. The dashed lines mark the possible cluster units of TM elements. Multiple clusters of random geometries and population are observed, confirming that no specific ordering exists in the superlattice scale. This is consistent with the previous experiments using X-ray diffraction and neutron diffraction characterization on $Li_{2/3}[Co_xNi_{1/3-x}Mn_{2/3}]O_2$ which demonstrated that Co suppressed the superlattice ordering when $x > 1/6$.[19] A special note on NMC333 is that the valence states for Ni and Co are dominantly Ni^{2+} and Co^{3+}. The radii difference of Ni^{2+} and Co^{3+}/Mn^{4+} is larger than 15% which may lead to the short-range pattern,[20−22] while the long-range ordering is compromised by the coexistence of Co^{2+} and Co^{3+}. We calculate the population of the TM−TM pairs in NMC333. Supporting Information Table S1 shows that indeed the TM elements distribute dispersedly in the short-range, and thus a $[\sqrt{3} \times \sqrt{3}]R30°$-type superlattice (in the Wood's notation) may exist for NMC333.[23]

Next, we study the electronic properties of NMC and seek to understand the interactions of aliovalent TM cations with O. According to the ligand field theory, the interaction between TMs and the ligand (O) is mainly σ-bonding with small contribution of π-bonding in the TM−O octahedral complex.[24] Supporting Information Figure S1 shows an example molecular

DOI: 10.1021/acs.jpcc.7b00810
J. Phys. Chem. C 2017, 121, 6002−6010

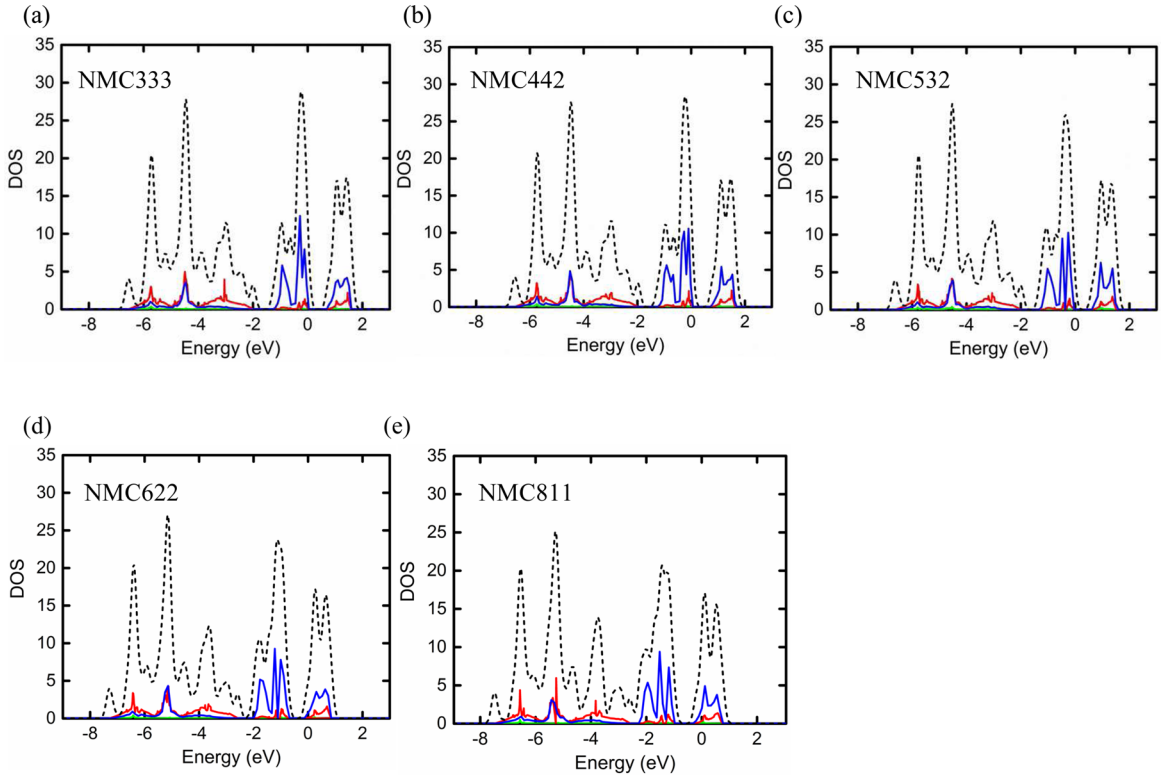

Figure 5. Total and partial density of states of (a) NMC333, (b) NMC442, (c) NMC532, (d) NMC622, and (e) NMC811, respectively. The dashed lines represent the total density of states. The blue, red, and green lines represent the partial density of states of the TM 3d orbital, O 2p orbital, and Li s orbital, respectively. Fermi energy is shifted to zero. Energy level below −4 eV shows large overlaps between O 2p and TM 3d orbitals due to the strong covalent interactions. The *t2g* population for the TM 3d orbital dictates the energy range of −2 to 0 eV. The higher energy region above the Fermi level represents the antibonding states between the *eg** population in the TM 3d orbital and partial O 2p orbital. The band gap gradually closes, and the Fermi energy shifts to larger values from NMC333 to NMC811 due to the increasing portion of Ni.

orbital diagram of the TM complex with the 3d orbital electron population of Co^{3+} and O 2p orbital. The *eg* level has a large overlap in the energy scale with the O 2p orbital and constitutes the covalent bonding orbital with a large coefficient for the ligand orbital. The three degenerated *t2g* orbitals, d_{xy}, d_{xz}, and d_{yz}, contribute to both the nonbonding and antibonding states. Other antibonding interactions are contributed by the two degenerated *eg** orbitals d_{z2} and $d_{x^2-y^2}$.[25] The orbital interactions are depicted in the plot of density of states (DOS). Figure 5 shows the total and partial DOS of the five NMC compositions. The dashed lines represent the total DOS. The blue, red, and green lines are the partial DOS of the TM 3d orbital, O 2p orbital, and Li s orbital, respectively. Fermi energy has been shifted to zero. Overall, there is little contribution of the Li s orbital in the energy range of −9−3 eV of the total DOS. Energy level below −4 eV shows a large overlap between the O 2p and TM 3d orbitals due to the strong covalent interactions. The *t2g* population for the TM 3d orbital dominates the energy range of −2 to 0 eV. The higher energy region above the Fermi level represents the antibonding states between the *eg** population in the TM 3d orbital and partial O 2p orbital. Comparing the DOS of the five NMC compounds, the Fermi energy shifts toward larger values when the Ni content increases because more valence electrons fill in the 3d orbital of Ni than Mn and Co. Furthermore, the band gap gradually closes from NMC333 to NMC811 indicating the metallic character of Ni-rich compounds. As discussed in Figure 3, when the Ni portion increases, more Ni transits to Ni^{3+} which increases the density of the electron/hole carriers and thus enhances the overall electrical conductivity.[26] Previous experimental measurements indeed showed a significant increase of electrical conductivity from NMC333 to NMC811 that is in good agreement with the DOS plot.[7] Another interesting fact that stronger JT distortion associated with the Ni-rich compound is also reflected in the density of states. The ligand field theory indicates that the distorted bond in TM octahedral complexes results in further splitting of the *t2g* orbitals, leading to the partial electron occupation at a lower energy level. Figure 5 shows that the peak value of the *t2g* orbital decreases with more DOS filling in between the lower valence regime and the *t2g* peak. The DOS at the *eg** level slightly decreases as well because of the transition from Ni^{2+} to Ni^{3+} from NMC333 to NMC811.

The comparative TM−O interactions can be revealed using the crystal orbital overlap population (COOP) analysis.[27] Figure 6 shows the COOP values for the TM−O pairs in NMC333. Positive values represent the bonding states, and negative values show the antibonding interaction. The broad positive regime around −5 eV corresponds to the strong covalent bonding between the *eg* level and the O 2p orbital. Around the Fermi level, the *t2g* level contributes to the antibonding and nearly nonbonding states at the Fermi level. In the conductive band, the COOP demonstrates the antibonding states between the *eg** level and partial O 2p orbital. At the Fermi level, the Co−O bond shows the minimum antibonding characteristic which might be related to the stable 3d-electron configuration of Co^{3+}. Besides, less antibonding in the conduction band is observed for Ni−O compared with Mn−O and Co−O. Mn−O exhibits the largest antibonding effect which may elongate the TM−O bonds in Mn-rich NMC compounds.

DOI: 10.1021/acs.jpcc.7b00810
J. Phys. Chem. C 2017, 121, 6002−6010

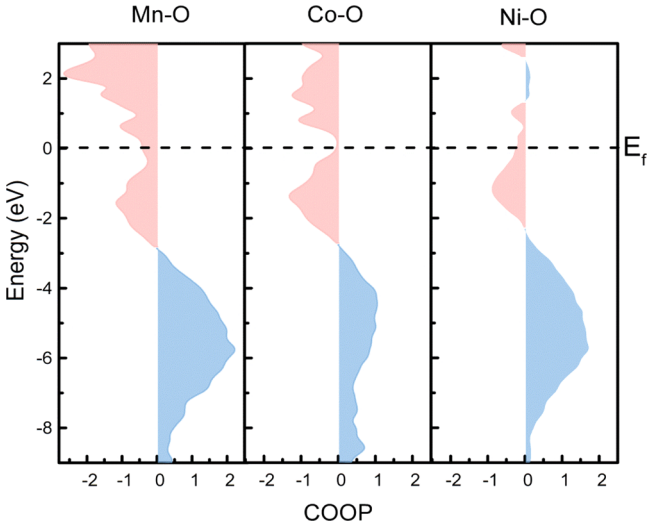

Figure 6. Crystal orbital overlap population analyses of the TM−O pairs. A positive value represents the bonding state, whereas a negative value shows the antibonding state. The broad bonding regime (−9 ∼ −4 eV) corresponds to the strong covalent states between TMs and O. Near the Fermi energy, the *t2g* level contributes to the antibonding states and nearly no bonding at the Fermi level. Above the Fermi energy, negative COOP indicates the repulsion of TMs and O because of the interactions of the *eg** level and O 2p orbital.

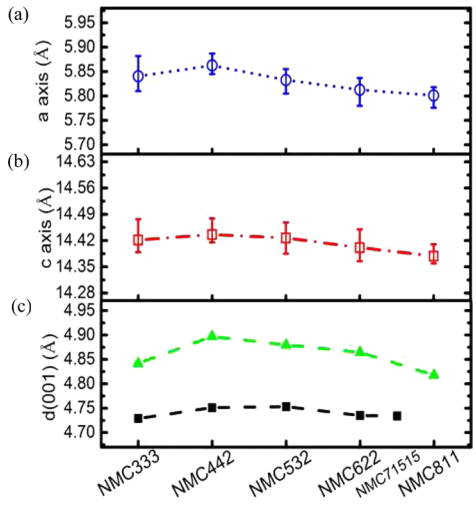

Figure 7. Lattice constants in (a) the *a*-axis and (b) the *c*-axis directions of the five NMC compositions. The average (symbols) and standard deviation (error bars) are calculated from the 81 configurations in each NMC composition. (c) Variation of the (001) plane spacing in different NMC compositions. The theoretical predictions (green line) show the same trend compared with the XRD measurement (black line).

The TM−O and TM−TM interactions determine the lattice parameters of NMC. A slight change in the lattice parameters has a significant effect on Li transport. It was predicted that when the Li slab space (Figure 2) increases by 0.1 Å the activation barrier of Li diffusion decreases by 100 meV.[28] Figure 7(a) and (b) shows the lattice constants in the *a*-axis and *c*-axis directions of the five NMC compositions, respectively. The average (symbols) and standard deviation (error bars) are calculated from the 81 configuration for each NMC composition. The lattice constants in both orientations show a similar parabolic behavior and reach maximum in NMC 442. Figure 7(c) plots the variation of the (001) plane distance in NMC in comparison with XRD measurements (black curve).[29] The (001) plane distance is the sum of the Li slab and TM slab distances (Figure 2). Although an ∼0.1 Å systematic difference exists in the theoretical calculation compared with the experimental results which is mostly due to the generalized gradient approximation (GGA) correlation functional adopted in the DFT calculation, their results follow exactly the same trend. The lattice constants increase from NMC333 to NMC442 and then gradually decrease with the rise of the Ni content. Table 2 gives more detailed information on the average TM−O and TM−TM pairs. As expected, the TM slab and Li slab distances follow the same trend of the (001) plane distance. The general decrease of the *c*-axis lattice constant is due to the weaker antibonding effect of the TM 3d orbital as we discussed in Figure 5 when the Ni content increases. Meanwhile, since NMC442 contains the largest content of Mn and the Mn−O has the strongest repulsive interaction, the *c*-axis lattice parameter reaches maximum in NMC442. The TM−TM distance determines the *a*-axis lattice parameter. The average lengths of Ni−Mn and Ni−Co pairs are relatively larger than that of Mn−Co due to the larger ionic radius of Ni. Since NMC442 has the largest mixing of Ni and Mn, a relatively larger value of *a*-axis lattice constant is expected.

Next, we explore the comparative mechanical, dynamic, and thermal properties of NMC materials and understand the electronic origin of the physicochemical properties. The finding that no long-range ordering is present in the TM layer of NMC allows us to use the virtual crystalline approximation (VCA) method which treats the TM elements as disordered alloying atoms (details in the Computational Methods).[30] The VCA model significantly reduces the computational cost and smoothly handles the stoichiometric variation in the five NMC compositions. Here we use both the supercell model and the VCA method to calculate the elastic modulus of NMC. Figure 8 shows the variation of Young's modulus in the five NMC compositions calculated by the two methods in comparison with the experimental values. The three solid lines show the Young's modulus calculated separately by VASP, CASTEP, and ABINIT. The green dots mark the experimental values of NMC333 and NMC532 measured by nanoindentation.[31−33] The theoretical predictions and experimental measurements quantitatively agree with each other. Elastic modulus monotonically decreases from NMC333 to NMC622 and then slightly increases in NMC811. Supporting Information Figure S2 shows the bulk modulus of the

Table 2. TM and Li Slab Spacing and Average Bond Length of TM−TM and TM−O Pairs

	slab spacing (Å)		average length (Å)					
NMC	TM layer	Li layer	Ni−Mn	Mn−Co	Ni−Co	Mn−O	Ni−O	Co−O
333	2.19	2.64	2.93	2.89	2.92	1.95	2.06	1.99
442	2.23	2.66	2.93	2.91	2.92	1.95	2.07	1.99
532	2.23	2.65	2.91	2.91	2.92	1.94	2.05	1.98
622	2.22	2.64	2.91	2.88	2.91	1.94	2.02	1.97
811	2.19	2.63	2.91	2.85	2.88	1.94	2.00	1.94

DOI: 10.1021/acs.jpcc.7b00810
J. Phys. Chem. C 2017, 121, 6002−6010

five NMC compositions calculated from the VCA model. NMC622 has the minimum values of both Young's modulus and bulk modulus. Mechanical properties are closely related with the electronic structure. The valence electron density (per atomic volume) determines the bulk modulus of materials, and a large valence electronic density will result in a high bulk modulus. From the DOS plot and the COOP analysis, we learn that the valence orbitals (*eg* level for TM and 2p for O) contribute to the covalent bonding of TM−O, and the *t2g* and *eg** levels contribute to the broad antibonding state. In the valence band (−9 ∼ −3 eV, Figure 5), all five NMC compositions have similar amount of valence electrons. Thus, the TM atomic size will be a determining factor on the valence electron density. Considering the difference in the Co stoichiometry is small and Mn remains the same valence state in the different compounds, the variation of atomic size is mainly controlled by Ni. As Ni has larger ionic radii compared to Co and Mn (Figure 1), the overall average atomic size increases when the Ni composition increases. Therefore, the valence electron density would generally decrease when the Ni content increases, and so does the bulk modulus. Nevertheless, the ionic size decreases when a number of Ni cations undergo the transition from 2+ to 3+ oxidation state from NMC333 to NMC811. The above two competing factors on the ionic size result in the

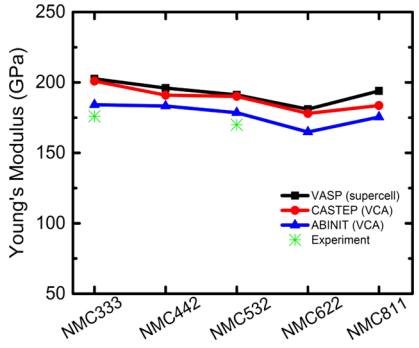

Figure 8. Young's modulus of the five NMC compositions calculated from the supercell model (VASP) and the virtual crystal approximation model (CASTEP and ABINIT) in comparison with the experimental values.

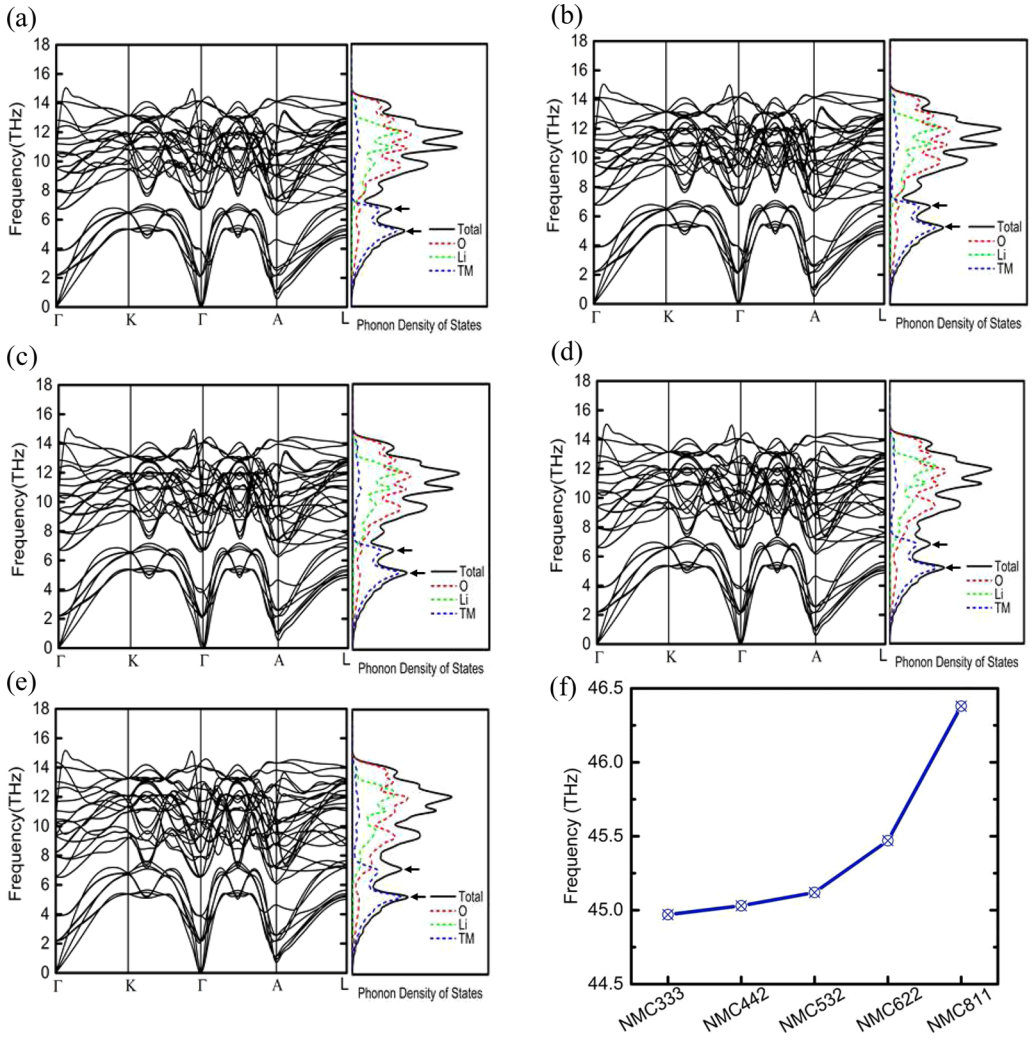

Figure 9. (a−e) Phonon dispersion and phonon density of states of NMC333, NMC442, NMC532, NMC622, and NMC811, respectively. In the phonon dispersion curves, the three lowest branches represent the acoustic mode, and the other 30 three branches represent the optical mode. In the DOS curves, the high- and medium-frequency regimes are contributed by Li and O, while the low-frequency regime is mainly contributed by TMs. From (a) to (e), the two peaks in the low-frequency regime sharpen and slightly shift toward higher values, indicating the increase of the TM−O bonding strength. (f) Longitude acoustic frequency in the five NMC compounds around the Gamma point. The acoustic frequency increases from NMC333 to NMC811 due to the weaker electron screening effect.

DOI: 10.1021/acs.jpcc.7b00810
J. Phys. Chem. C 2017, 121, 6002−6010

minimum valence electron density and modulus in NMC622—the difference in the elastic modulus between NMC333 and NMC622 is around 21 GPa.

On the dynamic properties, Figure 9(a)−(e) shows the phonon dispersion curves for the phonon population along the Γ−K−Γ−A−L path in the reciprocal space and the phonon density of states contributed by Li, O, and TMs in the five NMC compounds. The VCA model contains 12 atoms, and thus there are 3 acoustic branches and 33 optical branches in the phonon dispersion curves. The acoustic branches locate at the lowest energy regime. Figure 9 (f) shows that the longitudinal acoustic frequency around the Gamma point gradually increases from NMC333 to NMC811 due to the weaker electron screening effect when the electron DOS at the Fermi level decreases (Figure 5). Furthermore, the low phonon frequency branches (marked by two arrows in (a)−(e)) slightly move toward a higher-frequency regime when the Ni content increases. From the plot of phonon density of states, it shows that the medium and high-frequency regimes are contributed by Li and O, and the low-frequency regime is mainly contributed by the TM elements. The sharpening and shift of the two peaks in the low-frequency regime indicate the strengthening of the TM−O bonds in the Ni-rich compound, which is consistent with the general decreasing lattice constant in the *c*-axis.

We further calculate the thermal properties of NMC including the vibrational Helmholtz free energy *F*, the vibrational entropy *S*, and the constant-volume specific heat capacity C_V. Figure 10 shows the results in the range of 50−450 K. The

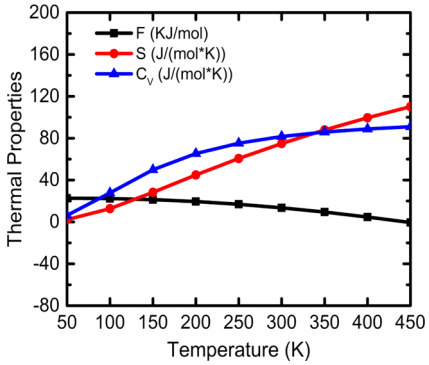

Figure 10. Thermal properties of NMC including the Helmholtz free energy *F*, the vibrational entropy *S*, and the constant-volume specific heat capacity C_V.

thermal properties of the five NMC compounds are nearly identical and are similar to $LiCoO_2$.[14] This is understood that the crystalline symmetry mainly determines the thermal properties. Both $LiCoO_2$ and the NMC lattice have the *R*3*m* space group, resulting in similar phonon vibration modes in the lattice. Figure 10 also shows that the heat capacity approaches to the classical Dulong−Petit asymptotic limit when the temperature increases to infinity. In the VCA model, the primitive cell contains four atoms. Thus, the constant-volume heat capacity approaches the limit value of 12*R* (99.7 J/mol/K, where *R* is the gas constant in the unit of J/mol/K) when temperature tends to the positive infinity.

Thermal stability of the electrodes is a key issue for the safe operation of Li-ion batteries. We show the correlation of calculated cohesive energies, defined as the energy required to break the compositions up into isolated free atoms, with the thermal stability of the five NMC compositions in Figure 11.

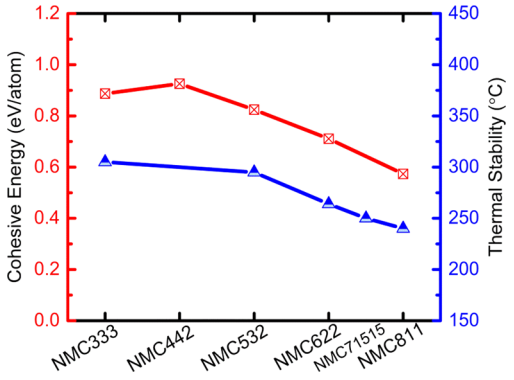

Figure 11. Thermal stability (experimental values, blue triangles) and cohesive energies (theoretical results, red rectangles) of the five NMC compositions. Thermal stability gradually degrades in the Ni-rich compounds.

Thermal stability is represented by the exothermic reaction peak temperature in the calorimetry experiments.[34] The cohesive energy steadily decreases when the Ni content increases which corroborates that the thermal stability degrades in the Ni-rich compounds. The thermal stability is also closely related with the structural stability as a stable structure will experience a high phase transition temperature. Thus, the JT effect we discussed earlier can be an indicator of the thermal stability. Recall that the JT distortion in NMC is mainly induced by the increasing portion of Ni^{3+}, and the degradation of thermal stability in the Ni-rich compounds is expected.

CONCLUSION

In conclusion, we study the electronic structure and valence states of TM elements in NMC cathode materials. The multivalence states Ni^{2+}/Ni^{3+} and Co^{2+}/Co^{3+} coexist, and their occupation fractions vary by the NMC composition. The variation of the valence states determines the comparative structural, electrical, mechanical, and thermal properties in NMC. Through detailed analysis on the molecular orbital interactions and bonding characteristics, we validate that NMC333 possesses the highest structural stability, thermal stability, and elastic modulus, while the electric conductivity is improved in the Ni-rich compounds. The theoretical predictions are in excellent agreement with the experimental results. Furthermore, we demonstrate that no long-range ordering exists in the TM layer of NMC through intensive computational screening. The first-principles theoretical studies provide fundamental understanding of the physicochemical properties at the intrinsic level of electronic structures and will offer important insight in the selection of NMC materials for enhanced electrochemical performance.

ASSOCIATED CONTENT

Supporting Information

The Supporting Information is available free of charge on the ACS Publications website at DOI: 10.1021/acs.jpcc.7b00810.

Table S1. Probability of TM−TM pairs in NMC333 (PDF)

AUTHOR INFORMATION

Corresponding Author

*E-mail: kjzhao@purdue.edu.

ORCID

Kejie Zhao: 0000-0001-5030-7412

DOI: 10.1021/acs.jpcc.7b00810
J. Phys. Chem. C 2017, 121, 6002−6010

Notes

The authors declare no competing financial interest.

■ ACKNOWLEDGMENTS

We are grateful for the supports by the Office of Naval Research through the NEPTUNE program and by the National Science Foundation through the grant CBET-1603866. K.Z. acknowledges helpful discussions with Dr. Peilin Liao and Dr. Jianlin Li.

■ REFERENCES

(1) Palacín, M.; de Guibert, A. Why do batteries fail? *Science* **2016**, *351*, 1253292.

(2) Rozier, P.; Tarascon, J. M. Review − Li-Rich Layered Oxide Cathodes for Next-Generation Li-Ion Batteries: Chances and Challenges. *J. Electrochem. Soc.* **2015**, *162*, A2490−A2499.

(3) Mohanty, D.; Li, J.; Nagpure, S. C.; Wood, D. L.; Daniel, C. Understanding the structure and structural degradation mechanisms in high-voltage, lithium-manganese−rich lithium-ion battery cathode oxides: A review of materials diagnostics. *MRS Energy & Sustainability* **2015**, *2*, E15.

(4) Ohzuku, T.; Makimura, Y. Layered Lithium Insertion Material of $LiNi_{1/2}Mn_{1/2}O_2$: A Possible Alternative to $LiCoO_2$ for Advanced Lithium-Ion Batteries. *Chem. Lett.* **2001**, *30*, 744−745.

(5) Lu, Z.; MacNeil, D.; Dahn, J. Layered $Li[Ni_xCo_{1-2x}Mn_x]O_2$ Cathode Materials for Lithium-Ion Batteries. *Electrochem. Solid-State Lett.* **2001**, *4*, A200−A203.

(6) Kim, M.-H.; Shin, H.-S.; Shin, D.; Sun, Y.-K. Synthesis and electrochemical properties of $Li[Ni_{0.8}Co_{0.1}Mn_{0.1}]O_2$ and $Li[Ni_{0.8}Co_{0.2}]O_2$ via co-precipitation. *J. Power Sources* **2006**, *159*, 1328−1333.

(7) Noh, H.-J.; Youn, S.; Yoon, C. S.; Sun, Y.-K. Comparison of the structural and electrochemical properties of layered $Li[Ni_xCo_yMn_z]O_2$ (x= 1/3, 0.5, 0.6, 0.7, 0.8 and 0.85) cathode material for lithium-ion batteries. *J. Power Sources* **2013**, *233*, 121−130.

(8) Etacheri, V.; Marom, R.; Elazari, R.; Salitra, G.; Aurbach, D. Challenges in the development of advanced Li-ion batteries: A review. *Energy Environ. Sci.* **2011**, *4*, 3243−3262.

(9) Xu, B.; Qian, D.; Wang, Z.; Meng, Y. S. Recent progress in cathode materials research for advanced lithium ion batteries. *Mater. Sci. Eng., R* **2012**, *73*, 51−65.

(10) Kresse, G.; Furthmüller, J. Efficient iterative schemes for ab initio total-energy calculations using a plane-wave basis set. *Phys. Rev. B: Condens. Matter Mater. Phys.* **1996**, *54*, 11169.

(11) Kresse, G.; Joubert, D. From ultrasoft pseudopotentials to the projector augmented-wave method. *Phys. Rev. B: Condens. Matter Mater. Phys.* **1999**, *59*, 1758.

(12) Zhou, F.; Cococcioni, M.; Marianetti, C. A.; Morgan, D.; Ceder, G. First-principles prediction of redox potentials in transition-metal compounds with LDA+ U. *Phys. Rev. B: Condens. Matter Mater. Phys.* **2004**, *70*, 235121.

(13) Bannikov, V. V.; Shein, I. R.; Ivanovskii, A. L. Elastic and electronic properties of hexagonal rhenium sub - nitrides Re_3N and Re_2N in comparison with hcp - Re and wurtzite - like rhenium mononitride ReN. *Phys. Status Solidi B* **2011**, *248*, 1369−1374.

(14) Du, T.; Xu, B.; Wu, M.; Liu, G.; Ouyang, C. Insight into the Vibrational and Thermodynamic Properties of Layered Lithium Transition-Metal Oxides $LiMO_2$ (M= Co, Ni, Mn): A First-Principles Study. *J. Phys. Chem. C* **2016**, *120*, 5876−5882.

(15) Shannon, R. t. Revised effective ionic radii and systematic studies of interatomic distances in halides and chalcogenides. *Acta Crystallogr., Sect. A: Cryst. Phys., Diffr., Theor. Gen. Crystallogr.* **1976**, *32*, 751−767.

(16) Czyżyk, M.; Potze, R.; Sawatzky, G. Band-theory description of high-energy spectroscopy and the electronic structure of $LiCoO_2$. *Phys. Rev. B: Condens. Matter Mater. Phys.* **1992**, *46*, 3729.

(17) Glass, C. W.; Oganov, A. R.; Hansen, N. USPEX—evolutionary crystal structure prediction. *Comput. Phys. Commun.* **2006**, *175*, 713−720.

(18) Kubota, K.; Asari, T.; Yoshida, H.; Yaabuuchi, N.; Shiiba, H.; Nakayama, M.; Komaba, S. Understanding the Structural Evolution and Redox Mechanism of a $NaFeO_2$−$NaCoO_2$ Solid Solution for Sodium - Ion Batteries. *Adv. Funct. Mater.* **2016**, *26*, 6047−6059.

(19) Lu, Z.; Donaberger, R.; Dahn, J. Superlattice ordering of Mn, Ni, and Co in layered alkali transition metal oxides with P2, P3, and O3 structures. *Chem. Mater.* **2000**, *12*, 3583−3590.

(20) Meng, Y.; Ceder, G.; Grey, C.; Yoon, W.-S.; Jiang, M.; Breger, J.; Shao-Horn, Y. Cation Ordering in Layered O3 $Li[Ni_xLi_{1/3-2x/3}Mn_{2/3-x/3}]O_2$ ($0 \leqslant x \leqslant 1/2$) Compounds. *Chem. Mater.* **2005**, *17*, 2386−2394.

(21) Meng, Y.; Ceder, G.; Grey, C.; Yoon, W.-S.; Shao-Horn, Y. Understanding the Crystal Structure of Layered $LiNi_{0.5}Mn_{0.5}O_2$ by Electron Diffraction and Powder Diffraction Simulation. *Electrochem. Solid-State Lett.* **2004**, *7*, A155−A158.

(22) Wang, Y.; Xiao, R.; Hu, Y.-S.; Avdeev, M.; Chen, L. P2-$Na_{0.6}[Cr_{0.6}Ti_{0.4}]O_2$ cation-disordered electrode for high-rate symmetric rechargeable sodium-ion batteries. *Nat. Commun.* **2015**, *6*, 6954.

(23) Karino, W. Order of the transition metal layer in $LiNi_{1/3}Co_{1/3}Mn_{1/3}O_2$ and stability of the crystal structure. *Ionics* **2016**, *22*, 991−995.

(24) Ballhausen, C. J. *Ligand field theory*; McGraw-Hill: New York, 1962; Vol. *256*.

(25) Doublet, M.-L. *Orbital Approach to the Electronic Structure of Solids*; Oxford University Press: 2012.

(26) Kickelbick, G. *Hybrid materials: synthesis, characterization, and applications*; John Wiley & Sons: 2007.

(27) Dronskowski, R.; Bloechl, P. E. Crystal orbital Hamilton populations (COHP): energy-resolved visualization of chemical bonding in solids based on density-functional calculations. *J. Phys. Chem.* **1993**, *97*, 8617−8624.

(28) Kang, K.; Meng, Y. S.; Bréger, J.; Grey, C. P.; Ceder, G. Electrodes with high power and high capacity for rechargeable lithium batteries. *Science* **2006**, *311*, 977−980.

(29) Cui, S.; Wei, Y.; Liu, T.; Deng, W.; Hu, Z.; Su, Y.; Li, H.; Li, M.; Guo, H.; Duan, Y.; Wang, W.; Rao, M.; Zheng, J.; Wang, X.; Pan, F. Optimized Temperature Effect of Li-Ion Diffusion with Layer Distance in $Li(Ni_xMn_yCo_z)O_2$ Cathode Materials for High Performance Li-Ion Battery. *Adv. Energy Mater.* **2016**, *6*, 1501309.

(30) Hua, G.; Li, D. A first-principles study on the mechanical and thermodynamic properties of $(Nb_{1-x}Ti_x)C$ complex carbides based on virtual crystal approximation. *RSC Adv.* **2015**, *5*, 103686−103694.

(31) Vasconcelos, L. S.; Xu, R.; Li, J.; Zhao, K. Grid indentation analysis of mechanical properties of composite electrodes in Li-ion batteries. *Extreme Mechanics Letters* **2016**, *9*, 495.

(32) Zeng, K.; Zhu, J. Surface morphology, elastic modulus and hardness of thin film cathodes for Li-ion rechargeable batteries. *Mech. Mater.* **2015**, *91*, 323−332.

(33) Kim, D.; Shim, H. C.; Yun, T. G.; Hyun, S.; Han, S. M. High throughput combinatorial analysis of mechanical and electrochemical properties of $Li[Ni_xCo_yMn_z]O_2$ cathode. *Extreme Mechanics Letters* **2016**, *9*, 439.

(34) Bak, S.-M.; Hu, E.; Zhou, Y.; Yu, X.; Senanayake, S. D.; Cho, S.-J.; Kim, K.-B.; Chung, K. Y.; Yang, X.-Q.; Nam, K.-W. Structural Changes and Thermal Stability of Charged $LiNi_xMn_yCo_zO_2$ Cathode Materials Studied by Combined In Situ Time-Resolved XRD and Mass Spectroscopy. *ACS Appl. Mater. Interfaces* **2014**, *6* (24), 22594−22601.

DOI: 10.1021/acs.jpcc.7b00810
J. Phys. Chem. C 2017, 121, 6002−6010